

Bolometric detection of Josephson radiation

Bayan Karimi,^{1,2} Gorm Ole Steffensen,^{3,4} Andrew P. Higginbotham,^{5,6}
Charles M. Marcus,^{7,8,9} Alfredo Levy Yeyati,³ and Jukka P. Pekola¹

¹*Pico group, QTF Centre of Excellence, Department of Applied Physics,
Aalto University, P.O. Box 15100, FI-00076 Aalto, Finland*

²*QTF Centre of Excellence, Department of Physics,
Faculty of Science, University of Helsinki, FI-00014 Helsinki, Finland*

³*Departamento de Física Teórica de la Materia Condensada,
Condensed Matter Physics Center (IFIMAC) and Instituto Nicolás Cabrera,
Universidad Autónoma de Madrid, 28049 Madrid, Spain*

⁴*Instituto de Ciencia de Materiales de Madrid (ICMM),
Consejo Superior de Investigaciones Científicas (CSIC),
Sor Juana Inés de la Cruz 3, 28049 Madrid, Spain*

⁵*The James Franck Institute and Department of Physics, University of Chicago, Chicago, IL 60637, USA*

⁶*IST Austria, Am Campus 1, 3400 Klosterneuburg, Austria*

⁷*Materials Science and Engineering and Department of Physics, University of Washington, Seattle WA 98195*

⁸*Center for Quantum Devices, Niels Bohr Institute,
University of Copenhagen, 2100 Copenhagen, Denmark*

⁹*InstituteQ – the Finnish Quantum Institute, Aalto University, Finland*

(Dated: February 15, 2024)

A Josephson junction (JJ) has been under intensive study ever since 1960's. Yet even in the present era of building quantum information processing devices based on many JJs, open questions regarding a single junction remain unsolved, such as quantum phase transitions, coupling of the JJ to an environment and improving coherence of a superconducting qubit. Here we design and build an engineered on-chip reservoir that acts as an efficient bolometer for detecting the Josephson radiation under non-equilibrium (biased) conditions. The bolometer converts ac Josephson current at microwave frequencies, up to about 100 GHz, into a measurable dc temperature rise. The present experiment demonstrates an efficient, wide-band, thermal detection scheme of microwave photons and provides a sensitive detector of Josephson dynamics beyond the standard conductance measurements. Using a circuit model, we capture both the current-voltage characteristics and the measured power quantitatively.

Understanding the dissipative dynamics of a Josephson junction (JJ) [1–6] has been a topic of intensive studies ever since the seminal theoretical works of Ivanchenko and Zil'berman [7] and of Caldeira and Leggett [8]. Nowadays, a JJ serves as a versatile component with a wide range of applications in various areas such as quantum computing and metrology [9]. Radiation from different types of JJs including semiconductor nanowires and thin-film microbridges has been detected by observing photon assisted tunneling, current-phase relationship, and properties of resonant cavities [10–17]. The concept of our experiment – converting ac Josephson current at microwave frequencies to measurable dc power – is based on nano-bolometric techniques [18–25]. We employ a hot-electron bolometer (HEB), which consists of a normal-metal nano-absorber whose temperature is measured by a normal-metal – insulator – superconductor (NIS) thermometer probe [26, 27]. Due to the quadratic response of the bolometer, simple dc measurement of the absorber temperature yields the magnitude of the Josephson current at frequencies up to about 100 GHz.

In the experiment, we simultaneously measure the average (charge) current through the junction and the HEB signal. The temperature of the HEB is able to resolve the transport characteristics of the Josephson junction with

high resolution, and it reveals complementary features as compared to those given by the dc charge transport characteristics. As a byproduct, we find that the ubiquitous drop of current at finite subgap voltage can be quantitatively explained by the shunting effect of the local environment of the junction.

The conventional picture of a current-biased Josephson junction (JJ) is that of a tilted washboard potential against the phase bias φ across it as in Fig. 1(a), where the slope is given by the bias. At small currents, the phase remains trapped in one of the wells of this potential, and since the voltage V is proportional to the time derivative of this phase, given by the Josephson relation as $V = \frac{\hbar}{2e} d\varphi/dt$, the junction remains in its zero-voltage supercurrent state. The current in the junction is thus dissipationless. Upon increasing the tilt of the potential, the phase starts to move from one well to the next lower one, producing a non-vanishing voltage, i.e. the process becomes dissipative. Each jump in phase from one well to the next lower one releases energy equal to $\Phi_0 I$, where $\Phi_0 = h/2e$ is the superconducting flux quantum and I is the average current. The current experiment deals, however, mainly with a voltage-biased configuration where the picture is less understood.

The current through the junction at non-vanishing

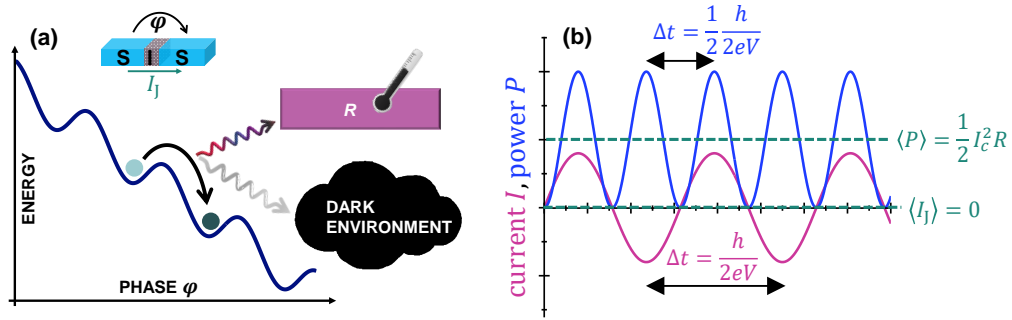


FIG. 1. Energy released from a biased superconductor-insulator-superconductor (SIS) Josephson junction. (a) The conceptual illustration of the energy vs. the phase drop φ across the biased JJ. This junction emits energy either to the engineered absorber on the chip R or to the dark environment. (b) The time average current $\langle I_J \rangle = 0$ vanishes ideally in a voltage-biased junction, whereas the average power remains non-vanishing.

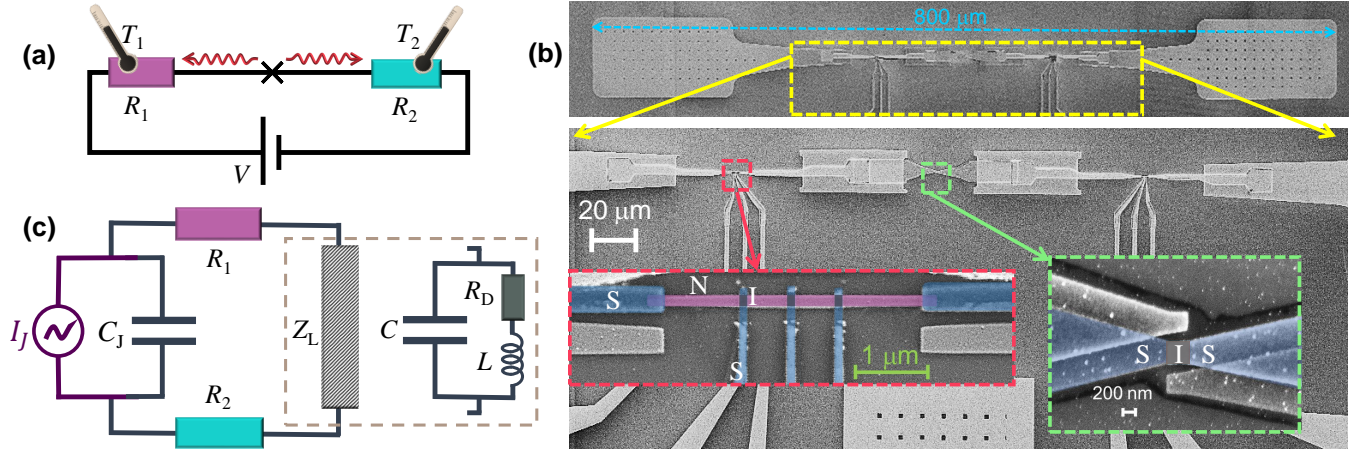


FIG. 2. A setup consisting of the JJ surrounded by two bolometers. (a) A schematic illustration of the device where the energy from the voltage V -biased JJ (cross shaped structure) at angular frequency $\omega_J = 2eV_{JJ}/\hbar$ is emitted to the two absorbers with resistances R_1 and R_2 . Here $V_{JJ} \simeq V$ is the voltage drop across the JJ. The thermometers on the absorbers measure the temperature changes of them, T_1 and T_2 , simultaneously. (b) A scanning electron micrograph of the device on different scales. A single JJ in the middle is sandwiched between two resistors placed at a distance of about $100 \mu\text{m}$ from the JJ. The connections are made with aluminum (Al) and with niobium (Nb, the wider sections). The zoomed-in views highlight the SIS junction (Al, blue; AlO_x , grey) in the middle (scale bar, 200nm) and the left side, one of the absorbers (resistor R_1) made of copper in purple color, in clean contact with Al (blue) leads (scale bar, $1 \mu\text{m}$) connecting to the patterned niobium film (light grey). The temperature of the absorber is monitored and controlled by three NIS probes (Cu/ AlO_x /Al). (c) Lumped-element model of the device for radio-frequencies; a single JJ represented by a current source I_J , an ideal Josephson element, and capacitance C_J in parallel. The load impedance Z_L is the termination of the device via bonding pads and wire bonds, and it is modelled as a dissipative LCR_D element as shown. Here R_D is the resistor representing the dark environment.

voltage is given by the Josephson relation, $I_J = I_c \sin \varphi$, where I_c is the junction-specific critical current, and the phase is evolving according to $\varphi(t) = 2eVt/\hbar$. The mean-squared value of this current is then given by $I_c^2/2$. The conceptual difference between the measurement of current and power is illustrated in Fig. 1(b). A key question is, can this alternating ac Josephson current be fully detected by the bolometer operating in dc mode, i.e., can we measure the power equal to $P = I_c^2 R/2$ via a temperature measurement of the resistor with resistance R ? We will first introduce the experimental setup and results, which allow us to answer this question affirmatively. The second key question in our work is: where does this energy

get absorbed? Can it be collected by a bolometric detector or is it released to an unknown environment which can not be monitored?

A schematic representation of the setup is shown in Fig. 2(a) where the energy is released by the JJ biased at voltage V , indicated by the cross. As will be clear in what follows, the bias voltage V is dropping almost fully across the junction except in the trivial supercurrent branch. Therefore we do not make a distinction between the two, and use V to denote both. The temperatures T_1 and T_2 , of the absorbers are measured by the thermometers attached to them. Figure 2(b) displays the actual device, where a single JJ in the middle is po-

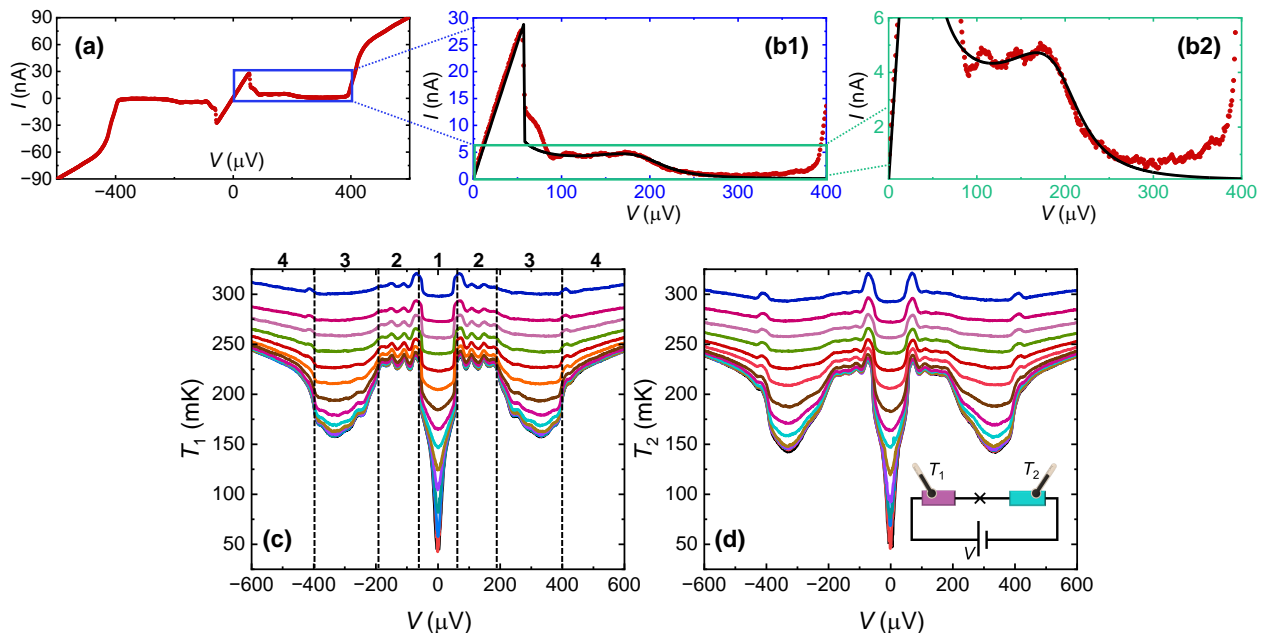


FIG. 3. Transport characteristics of the device of Fig. 2(b). (a) The I - V characteristic shown with red symbols measured at $T = 50$ mK. (b1),(b2) Zoom-in of the enclosed area in blue shown in panel (a). The black solid line is from the theoretical model with parameters: $R_1 + R_2 = 30 \Omega$, $R_D = 120 \Omega$, $R_S = 1920 \Omega$, $C_J = 15$ fF, $C = 40$ fF, $L = 2.1$ nH, and $I_c = 64$ nA. (c),(d) Simultaneous measurement of the temperature of the two resistors (T_1 and T_2) as a function of applied bias V .

sitioned between two normal metal resistors R_1 and R_2 , made of copper, working as absorbers, at a distance of about $100 \mu\text{m}$ symmetrically around the JJ. The connections are made of aluminum whose thermal conductance is negligible at low temperatures [1, 28]. By current-biasing a pair of normal-metal – insulator – superconductor junctions (SINIS) attached by superconducting leads to the resistors, one can control and monitor their temperatures. The voltage across the junction at a fixed bias current measured at different bath temperatures yields the temperature calibration in a standard way as presented in the Supplementary Material. The resistance of each resistor is about 15Ω . The simplified equivalent circuit of the device, used in the theoretical modeling of the I - V characteristics and power, is presented in Fig. 2(c). Here a single JJ is represented by an ac current source in parallel with capacitance C_J , and Z_L is the external impedance formed mainly by the bonding pads and wires.

TABLE I. Different bias regimes

Regime	Range of $ V $	Process
Regime 1	$< 50 \mu\text{V}$	supercurrent
Regime 2	$50 - 200 \mu\text{V}$	Josephson radiation I $\omega < \omega_{LC}$
Regime 3	$200 - 400 \mu\text{V}$	Josephson radiation II $\omega > \omega_{LC}$
Regime 4	$> 400 \mu\text{V}$	quasiparticle current

The I - V characteristic of the device at $T = 50$ mK is presented in Fig. 3(a). In the supercurrent branch in the central part, the positive constant slope is a result of the series resistance R_S from the two absorbers, the load resistors on the chip, and line resistance from room temperature to the chip ($R_S \approx 1920 \Omega$) as we do a two-wire measurement. The almost flat section up to the gap, $V = 2\Delta/e \simeq 400 \mu\text{V}$, is followed by a rise in current, transitioning into a quasiparticle current with specific resistance of the JJ, $R_T = 5.0 \text{ k}\Omega$. The magnified view of the enclosed area of the I - V characteristic in panel (a), as displayed in Figs. 3(b1) and 3(b2), provides a closer look at this measurement. It unveils additional details, particularly the oscillations between $|V| = 50 - 200 \mu\text{V}$ and drop in current at $|V| = \Delta/e \simeq 200 \mu\text{V}$ in the subgap regime.

We now analyze theoretically the I - V profile in the almost flat subgap region, $50 \mu\text{V} \lesssim V \lesssim 400 \mu\text{V}$, in terms of an underdamped JJ in series with a frequency dependent impedance $Z(\omega)$. In this regime, the phase evolves as

$$\varphi(t) \approx \omega_J t + \frac{2e I_c |Z(\omega_J)|}{h \omega_J} \sin(\omega_J t + \delta) \quad (1)$$

with the phase shift $\delta = -\arctan(\text{Re}Z(\omega_J)/\text{Im}Z(\omega_J))$. To the lowest order in voltage variations across the junction, the JJ dc current $I \equiv \langle I_J \rangle$ and voltage drop are given by,

$$I = I_c \frac{e}{h} \frac{\text{Re}Z(\omega_J)}{\omega_J}, \quad V = \frac{h}{2e} \omega_J + Z(0)I, \quad (2)$$

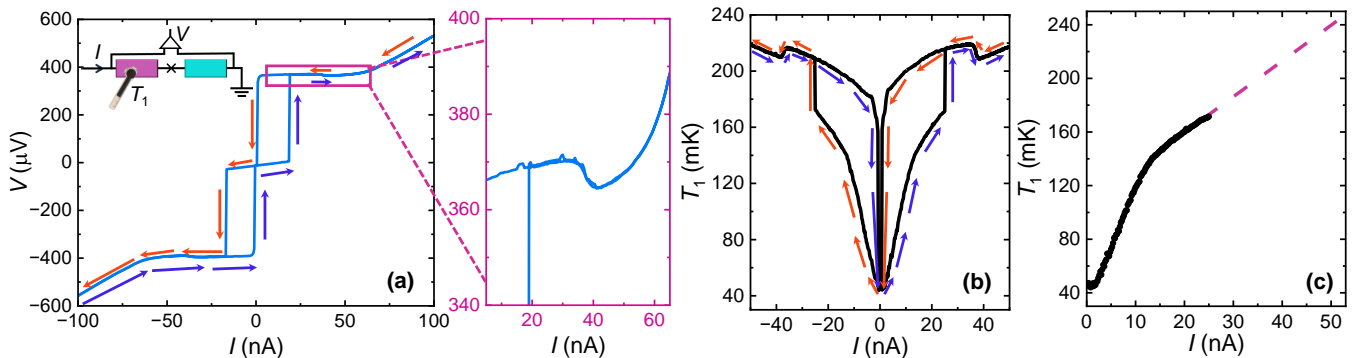


FIG. 4. Characteristics of the current-biased JJ. (a) Hysteretic $V - I$ characteristics of the junction together with a zoom in the quasiparticle branch. The blue arrows display the signal in the forward current sweep while the red ones present the reverse sweep. The setup for voltage and temperature measurement is shown in the inset. (b) Measured resistor temperature at current bias of $I_{1,\text{th}} = 15$ pA at $T_0 = 43$ mK. The nearly parabolic bottom in the small bias range corresponds to the hysteretic supercurrent branch of the single JJ. (c) The data in the supercurrent branch presented in panel (b) at positive currents. The dashed line indicates the linear extrapolation in the regime not reachable by the supercurrent measurement.

which is solved to yield the $I-V$. Intuitively, the proportionality of I on $Z(\omega)$ arises from the dynamics of the phase particle in the washboard potential. The lower the friction, given by $Z(\omega)$, more uniformly the phase runs down the washboard resulting ideally in vanishing $I = I_c \langle \sin \varphi(t) \rangle_0$, while larger friction results in a more rugged motion of it, thereby increasing I . Here the subscript 0 denotes the average over the period. The $I-V$ seen in Figs. 3(b) is reproduced by using the impedance of the ac circuit, containing a LC resonance, $\omega_{LC}/2\pi \approx 100$ GHz. More details on the theory can be found in the Supplementary Material. This model captures the main features of the experimental $I-V$ curve with realistic circuit parameters as shown by black lines in Figs. 3(b1) and 3(b2).

The energy released from the JJ at the given voltage bias is absorbed partly or fully by the two resistors. The measurement of temperatures T_1 and T_2 as a function of applied bias V is presented in Figs. 3(c) and 3(d), respectively, see also additional data for another sample in Fig. 7. The temperature calibration is explained in the Supplementary Material. The non-monotonic behavior of temperatures is remarkably similar in the two absorbers. The temperature changes clearly indicate four different regimes based on the different sections of the $I-V$ characteristic presented in panels 3(a) and 3(b). These regimes are summarized in Table 1. In the central region, Regime 1 up to $|V| \simeq 50 \mu\text{V}$, the entire heating of the resistors is attributed to Joule heating, a consequence of the current flowing through the resistors, as there is no power dissipation within the Josephson junction itself. The most interesting regime, Regime 2, lies within the intermediate range, $50 \mu\text{V} < |V| < 200 \mu\text{V}$, where the energy released by the ac Josephson current at the frequency $f = 2eV/h$ is absorbed by the resistors. In this regime, the temperature is high and shows small oscillations as

a function of I , as discussed below and in the additional data of Fig. 6. In Regime 3, $200 \mu\text{V} < |V| < 400 \mu\text{V}$, the power emitted into the two resistors decreases, corresponding to reduction in their temperatures. At high voltage bias $|V| > 400 \mu\text{V}$, Regime 4, in the quasiparticle branch, only a small fraction of power generated within the junction is dissipated into the two absorbers leading to a continuous, monotonous increase in their temperatures. Note that power generated at the junction in Regime 4, based on the dc $I-V$, is indeed more than 100 times higher than in Regime 2, but the temperature rise is comparable indicating a different mechanism of heat transport in each regime.

The oscillations in Regime 2, spaced by about $\Delta V = 50 \mu\text{V}$, seen in Figs. 3(c) and 3(d) and expanded in the additional data in Fig. 6, can be qualitatively understood as follows. The whole device is about $800 \mu\text{m}$ long as shown in the top of Fig. 2(b). It acts as a cavity with imperfect termination. This termination by bonding pads and inductive bonding wires causes partial reflection of current leading to temperature variations in the absorbers visible in the subgap regime. The inset of the additional data in Fig. 6 displays the temperature variation of the absorber 1 within the subgap regime. The blue arrows point to the minima of the measured temperature. The main panel of this figure shows the positions of the minima in both absorbers representing perfect coincidence of the two.

Our qualitative interpretation of the overall temperature characteristics in Figs. 3(c) and 3(d) and in the inset of Fig. 6 is as follows. Beyond the pure Joule heating of the resistors by the dc current in Regime 1, the high level of heating in Regime 2 is attributed to the absorption of the ac-supercurrent-induced high-frequency ($2eV/h$) power in the corresponding resistor. As shown below, this dc power is very close to the average value $P_i = \frac{I^2}{2} R_i$ for $i = 1, 2$. Crossover to Regime 3 is characterized by

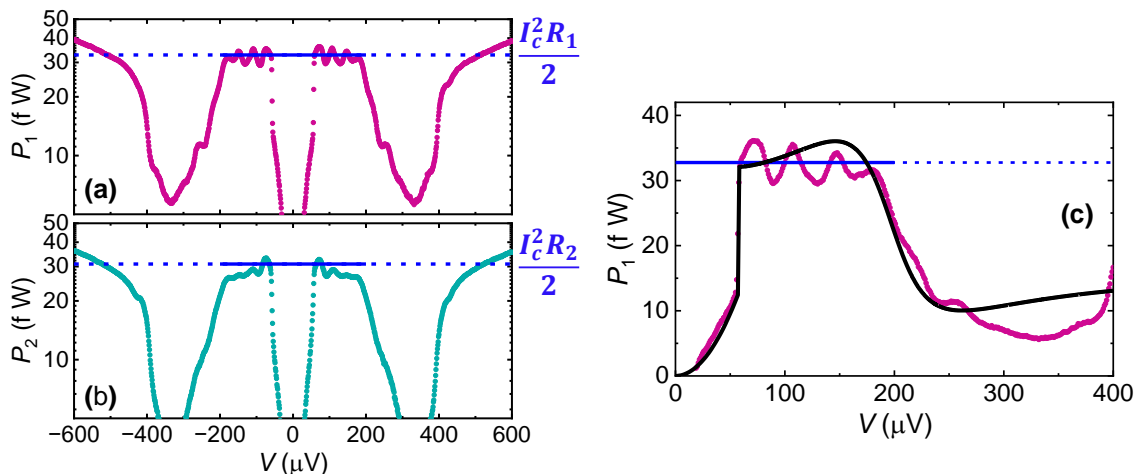


FIG. 5. The power P_i for $i = 1, 2$ as a function of the applied voltage V , obtained from the temperature measurement T_i for the two bolometers (Figs. 3(c) and 3(d)) at $T_0 = 43$ mK are shown in panels (a) and (b). The conversion from T to I is obtained from the calibration presented in Fig. 4(c). The horizontal blue line in each panel corresponds to $I_c^2 R_i/2$. (c) In this panel we have included the theoretical model, Eq. (3), to (a) using the same parameter values as for the I - V characteristic measurement presented in Fig. 3.

an abrupt decrease of power for both resistors. This drop has been seen in all the samples that we have measured, and it can be accounted by the drop in the current I : the circuit re-routes the current away from the thermometers at higher frequencies.

To understand this mechanism of re-routing we note that based on our circuit model (Fig. 2(c)), the power deposited in the HEBs in the underdamped regime is given by,

$$P_i = R_i I^2 + \frac{R_i I_c^2}{2} \left[(1 + C_J \omega_J \text{Im}Z(\omega_J))^2 + (C_J \omega_J \text{Re}Z(\omega_J))^2 \right], \quad (3)$$

which for small biases results in $P_I \approx \frac{R_i I_c^2}{2}$, but for biases $V \gg \frac{\hbar}{2e} \omega_{LC}$ the power approaches $P_i \approx \frac{R_i I_c^2}{2} \frac{1}{(1+C_J/C)^2}$. This is a consequence of the ac current bypassing the HEBs by running through C and C_J , instead of L , at large frequencies. Regime 4 represents pure quasiparticle current in tunneling, where the heat is released to the electrodes right at the junction in form of hot quasiparticles. These non-equilibrium quasiparticles diffuse poorly in the superconductor and do not carry heat to the resistors as effectively as Josephson radiation does.

The hysteretic measurement in the current biased configuration, presented in Fig. 4(a) gives us a way to perform the power calibration for the HEB. The key to this calibration is the measurement of the rise of the temperatures of the resistors R_i in the supercurrent branch of the Josephson junction, where there is no dissipation in the junction, and all the power is the plain Joule heating by the dc current through the corresponding resistor. The data from one of them as a function of current I is shown at $T_0 = 43$ mK in Fig. 4(b). The blue arrows

mark the current sweep in the forward direction, whereas the red ones denote the reverse direction. The hysteretic range at low currents corresponds to the non-dissipative supercurrent branch of the single JJ. Interestingly, we also see a drop in temperature at about 35 nA in the non-hysteretic quasiparticle branch. The $V - I$ shown in Fig. 4(b) and its inset demonstrates a drop at the same value of current, consistent with reduced heating above 35 nA. This drop could be associated with the “back-bending” behavior that has been observed in superconducting tunnel junctions [31, 32] due to a suppression of the gap caused by the non-equilibrium distribution of the tunneling quasiparticles.

In Fig. 4(c), we present the measurement of temperature for positive currents only. To reach the temperatures in all the relevant ranges, we perform a linear extrapolation. Now having the relation between I and T_i , we can convert each measured temperature T_i to effective power also in the voltage biased configuration. The above calibration allows us to convert temperature plots presented in Figs. 3(c) and 3(d) to power injected to the resistor, $P_i = I^2 R_i$ for $i = 1, 2$, as a function of bias voltage as presented in Figs. 5(a) and 5(b). The maximum power injected in the subgap regime is about 35 fW in each resistor. This power corresponds to about 25% of IV at low bias voltages.

The single JJ in the voltage biased configuration produces an ac Josephson current. We may compare the measured power to that expected if the ac Josephson current would produce Joule heating of resistor i at the rate $P_i = I_c^2 R_i/2$, stipulated by the condition that all this current would pass through this purely resistive absorber. The copper wire can indeed be considered as a resis-

tive element as its inductance and the capacitance across are small enough at the relevant microwave frequencies (< 100 GHz). The critical current can be obtained from the Ambegaokar-Baratoff formula [30], $I_c = \pi\Delta/(2eR_T)$, applicable at temperatures far below the critical temperature $T_c \approx 1.3$ K as in our experiment. The junction parameters were determined from the I - V curve of the JJ, with values $\Delta/e = 210 \mu\text{V}$ and $R_T = 5.0 \text{ k}\Omega$, yielding $I_c = 64 \text{ nA}$. With this procedure we obtain the expected powers $P_1 = 37 \text{ fW}$ and $P_2 = 35 \text{ fW}$, indicated by the blue horizontal lines in Fig. 5, in good agreement with the maximum sub-gap power in the experiment. The result of the theoretical model is shown by the solid black line in Fig. 5(c). Using the same parameter values as in Fig. 3, the full theoretical model captures the main features of the bias dependence in the experiment.

In this article, we have demonstrated experimentally bolometric detection of ac Josephson current. It is a complementary dc method with respect to measuring the I - V characteristics: the standard I - V or conductance measurement essentially averages the sinusoidal current, whereas the HEB measurement is quadratic in current, thus rectifying and fully retaining the ac component. This way, still by a simple dc measurement, we gain access to fine details of ac characteristics, which are largely averaged out and thus unreachable in the standard transport measurements. We presented a theoretical model that agrees with the experimental results using realistic circuit parameter values. It also gives a way to estimate the value of R_D , which presents the unknown dark environment. Our model also shows that one could improve the detection efficiency of the HEB by increasing its resistance as this quantity scales approximately as $(R_1 + R_2)/(R_D + R_1 + R_2)$.

ACKNOWLEDGMENTS

We thank Mikko Möttönen, Diego Subero, Vasilii Vadimov, Arman Alizadeh, Christoph Strunk, Nicolas Roch, Sergey Kafanov, Sergey Kubatkin, Andrew Kerman, and Joonas Peltonen for scientific discussions and Ze-Yan Chen for technical assistance. This work was funded by the Research Council of Finland Centre of Excellence program grant 336810 and grants 349601 (THEPOW). G. S. and A. L. Y. acknowledge financial support from the Spanish Ministry of Science through Grant TED2021-130292B-C43 funded by MCIN/AEI/10.13039/501100011033, "ERDF A way of making Europe" and the EU through FET-Open project AndQC. A. H. acknowledges support from the NOMIS foundation. C. M. M. acknowledges support from the Danish National Research Foundation and a research grant (Project 43951) from VILLUM FONDEN. We thank the facilities and technical support of Otaniemi research infrastructure for Micro and Nanotechnologies

(OtaNano).

-
- [1] B. D. Josephson, Possible new effects in superconductive tunnelling, *Phys. Lett.* **1**, 251 (1962).
 - [2] Ivar Giaever, Detection of the ac Josephson Effect, *Phys. Rev. Lett.* **14**, 904 (1965).
 - [3] Michael Tinkham, *Introduction to Superconductivity*, 2nd Edition (Dover Publications, 2004).
 - [4] M. H. Devoret, J. M. Martinis, and J. Clarke, Measurements of macroscopic quantum tunneling out of the zero-voltage state of a current-biased Josephson junction, *Phys. Rev. Lett.* **55**, 1908 (1985).
 - [5] D. Vion, M. Gotz, P. Joyez, D. Esteve, and M. H. Devoret, Thermal activation above a dissipation barrier: Switching of a small Josephson junction, *Phys. Rev. Lett.* **77**, 3435 (1996).
 - [6] A. A. Golubov, M. Yu. Kupriyanov, and E. Il'ichev, The current-phase relation in Josephson junctions, *Rev. Mod. Phys.* **76**, 411 (2004).
 - [7] Yu. M. Ivanchenko and L. A. Zil'berman, The Josephson effect in small tunnel contacts, *Sov. Phys. JETP* **28**, 1272 (1969).
 - [8] A. O. Caldeira and A. J. Leggett, Quantum Tunnelling in a Dissipative System, *Annals of Physics* **149**, 374 (1983).
 - [9] *Josephson Junctions for Metrology Applications, Fundamentals and Frontiers of the Josephson Effect*, edited by Francesco Tafuri (Springer New York, 2019).
 - [10] N. F. Pedersen, O. H. Soerensen, J. Mygind, P. E. Lindelof, M. T. Levinsen, and T. D. Clark, Direct detection of the Josephson radiation emitted from superconducting thin-film microbridges, *Appl. Phys. Lett.* **28**, 562 (1976).
 - [11] O. H. Soerensen, J. Mygind, N. F. Pedersen, V. N. Gubankov, M. T. Levinsen, P. E. Lindelof, Nonresonant detection of Josephson radiation from thin-film microbridges, *J. Appl. Phys.* **48**, 5372 (1977).
 - [12] David J. van Woerkom et al., Josephson radiation and shot noise of a semiconductor nanowire junction, *Phys. Rev. B* **96**, 094508 (2017).
 - [13] R. Haller et al., Phase-dependent microwave response of a graphene Josephson junction, *Phys. Rev. Research* **4**, 013198 (2022).
 - [14] L. Bretheau, Ç. Ö. Girit, H. Pothier, D. Esteve, and C. Urbina, Exciting Andreev pairs in a superconducting atomic contact, *Nature* **499**, 312 (2013).
 - [15] L. Bretheau, Ç. Ö. Girit, C. Urbina, D. Esteve, and H. Pothier, Supercurrent Spectroscopy of Andreev States, *Phys. Rev. X* **3**, 041034 (2013).
 - [16] R. S. Deacon et al., Josephson Radiation from Gapless Andreev Bound States in HgTe-Based Topological Junctions, *Phys. Rev. X* **7**, 021011 (2017).
 - [17] R. Haller, M. Osterwalder, G. Fülöp, J. Ridderbos, M. Jung, and C. Schönenberger, ac Josephson effect in a gate-tunable Cd_3As_2 nanowire superconducting weak link, *Phys. Rev. B* **108**, 094514 (2023).
 - [18] K. D. Irwin and G. C. Hilton, Transition-edge sensors. In: C. Enss, editor. *Cryogenic particle detection* (Berlin, Heidelberg: Springer; 2005).
 - [19] P. L. Richards, Bolometers for infrared and millimeter waves, *J. Appl. Phys.* **76**, 1 (1994).

- [20] Bayan Karimi, Fredrik Brange, Peter Samuelsson, and Jukka P. Pekola, Reaching the ultimate energy resolution of a quantum detector, *Nat. Commun.* **11**, 367 (2020).
- [21] R. Kokkonen et al., Bolometer operating at the threshold for circuit quantum electrodynamics, *Nature* **586**, 47 (2020).
- [22] Dmitry V. Morozov, Alessandro Casaburiand and Robert H. Hadfield, Superconducting photon detectors, *Contemporary Physics*, **62:2**, 69 (2021).
- [23] Evan D. Walsh et al., Josephson junction infrared single-photon detector, *Science* **372**, 409 (2021).
- [24] E. Gümüş et al., Calorimetry of a phase slip in a Josephson junction, *Nat. Phys.* **19**, 196 (2023).
- [25] A. Ibabe, M. Gómez, G. O. Steffensen, T. Kanne, J. Nygård, A. Levy Yeyati, and E. J. H. Lee, Joule spectroscopy of hybrid superconductor–semiconductor nanodevices, *Nat. Commun.* **14**, 2873 (2023).
- [26] M. Nahum and J. M. Martinis, Ultrasensitive-hot-electron microbolometer, *Appl. Phys. Lett.* **63**, 3075 (1993).
- [27] Francesco Giazotto, Tero T. Heikkilä, Arttu Luukanen, Alexander M. Savin, and Jukka P. Pekola, Opportunities for mesoscopics in thermometry and refrigeration: Physics and applications, *Rev. Mod. Phys.* **78**, 217 (2006).
- [28] J. T. Peltonen, P. Virtanen, M. Meschke, J. V. Koski, T. T. Heikkilä, and J. P. Pekola, Thermal Conductance by the Inverse Proximity Effect in a Superconductor, *Phys. Rev. Lett.* **105**, 097004 (2010).
- [29] Jukka P. Pekola and Bayan Karimi, Colloquium: Quantum heat transport in condensed matter systems, *Rev. Mod. Phys.* **93**, 041001 (2021).
- [30] Vinay Ambegaokar and Alexis Baratoff, Tunneling Between Superconductors, *Phys. Rev. Lett.* **10**, 486 (1963).
- [31] J. T. C. Yeh and D. N. Langenberg, Gap suppression by self-injection of quasiparticles in tin–tin-oxide–tin tunnel junctions, *Phys. Rev. B* **17**, 4303 (1978).
- [32] D. Winkler and T. Claeson, Non-Equilibrium Superconductivity in Aluminium Tunnel Junctions by Self-Injection and Millimeter Wave Radiation, *Phys. Scr.* **32**, 317 (1985).

METHODS

Fabrication: Our process consists of three steps: fabricating (i) the Nb patterned ground planes, (ii) single SIS JJ, and (iii) absorbers and thermometers. The devices were fabricated on highly resistive $675\ \mu\text{m}$ thick silicon substrates onto which a 40 nm aluminum-oxide layer by atomic layer deposition has been grown. Next it is coated with 200-nm-thick sputtered niobium film. Broader features such as contact leads and bonding pads were patterned by reactive ion etching (RIE) using CF_6+Ar chemistry on an electron-beam lithography-defined mask. The Josephson junction and NIS tunnel junctions were fabricated using a two-step process. First, shadow-mask electron-beam lithography was employed to pattern them onto a 950-nm-thick poly(methyl-metacrylate)/copolymer resist bilayer. This step was followed by developing the exposed structures in methyl-isobutyl-ketone (MIBK) in isopropanol (IPA) developer

and methylglycol-methanol solution for making undercuts, respectively.

Next, the junctions were deposited using the standard Dolan bridge technique by an electron-beam evaporator. Prior to metal evaporations, *in-situ* argon plasma milling was conducted on the sample surface. This milling process aimed to remove the native oxide layer, providing a pristine interface between the Nb and Al layers. In the first step, two-angle deposition process of 30-nm-thick Al layers with intermediate *in-situ* oxidation are performed to realize the single Josephson junction with tunnel resistance of $5\ \text{k}\Omega$ at mK temperatures.

The bolometers are made in the second step as shown in Fig. 2, similar to the preceding step. The procedure initiates with *in-situ* Ar ion plasma milling to ensure a clean contact between Nb and the deposited metals. The procedure then continues by first depositing a 20-nm-thick Al layer and *in-situ* oxidation, followed by a 30-nm-thick Cu layer, and finally by a 50-nm-thick Al layer in clean contact with the Cu layer. The typical tunnel junction resistance for NIS for this experiment is about $20\ \text{k}\Omega$. These NIS electrodes (probes) are connected to bonding pads for the setting and readout of the electronic temperature of the absorbers (R_1 and R_2).

The final stage of the fabrication is lift-off in acetone (52 degrees for $\sim 20 - 30$ min) and cleaning in isopropyl alcohol. After the fabrication process the device is bonded with Al wires to a custom-made brass chip carrier for the cryogenic characterization.

ADDITIONAL INFORMATION

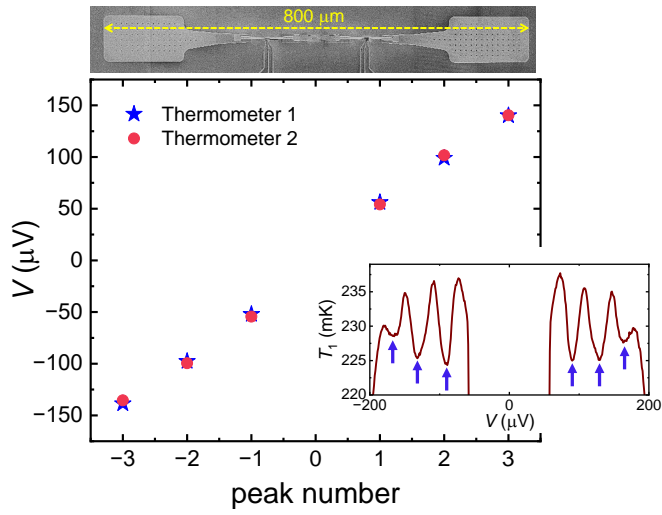


FIG. 6. Temperature resonances in the JJ cavity. Extracted voltage bias points V versus the peak number of both bolometers presented in Figs. 3(c) and 3(d). The inset shows a magnified view of the bias dependent temperature of R_1 at base temperature $T_0 = 43$ mK. The arrows point to the minima in temperature that have been extracted to the main panel.

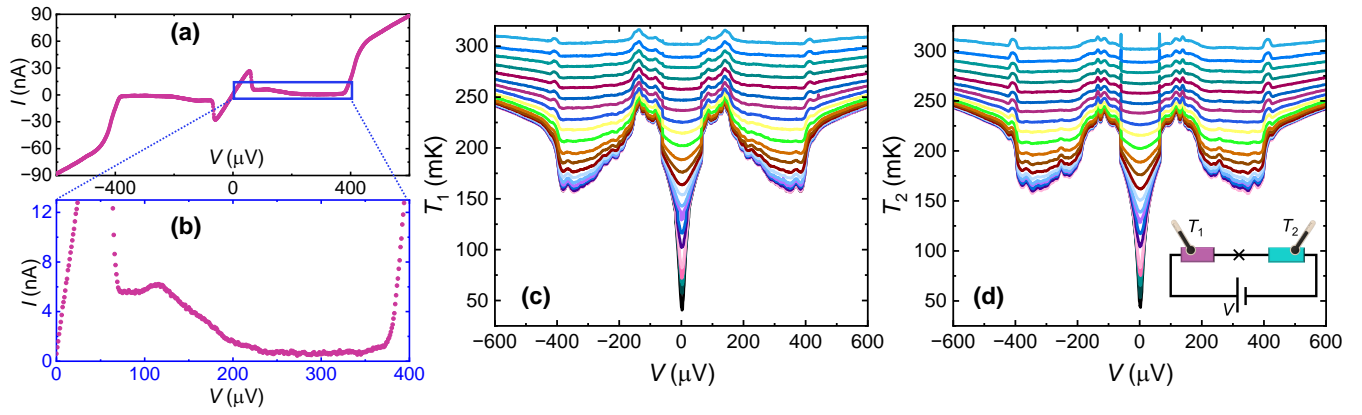


FIG. 7. Similar data as in Fig. 3, but here measured on another sample with nominally same parameters as those of the sample in the main text but with different wire-bonding conditions.

Supplementary Material

TEMPERATURE CALIBRATION

A pair of NIS-junctions attached to each resistor R_i serves as a thermometer. We apply a constant current $I_{\text{th},i}$ through this pair and measure the voltage across it [1], see Figs. A.1 and A.2. The calibration is done under equilibrium when the JJ bias current (and voltage) are set to zero. Under these conditions we assume that the electronic temperature of R_i equals that of the cryostat, measured independently using a calibrated RuO_x thermometer. Figures A.1 and A.2 are examples of the calibrations for the data in the main text.

THEORY AND FITTING DETAILS

In this section we add more detail to the theory utilized to fit the experiment in the main text, and we explain how the fitting is performed. We limit ourselves to a classical description of the circuit, and neglect effects of finite temperature and electrical noise, which we expect to play only a minor role.

As in the main text we describe the experimental circuit via lump elements, with the full circuit shown in Fig. A.3(a) with the dashed area indicating elements associated with the device, with the rest associated to the larger circuit external to the chip. Here C_B , which describes the contacts on the sample stage outside the chip, is assumed to be very large, $C_B \rightarrow \infty$, which separates the impedance into a zero-frequency part, $Z(\omega = 0) = R_1 + R_2 + R_S$, and a finite frequency part as

$$Z(\omega) = \left[iC_J\omega + \frac{1}{R_1 + R_2 + Z_{LC}(\omega)} \right]^{-1}, \quad (4)$$

$$Z_{LC}(\omega) = \left[iC\omega + \frac{1}{iL\omega + \frac{R_S R_D}{R_S + R_D}} \right]^{-1} \quad (5)$$

The full impedance is plotted in Fig. A.3(b), using the same parameters as the fit in the main text. The main features of this impedance is a LC resonance, $\omega_{LC} \approx \frac{1}{\sqrt{L(C+C_J)}}$, which is broadened mainly by R_D . Before the resonance, $\omega \ll \omega_{LC}$, the real part of the impedance saturates at $Z(\omega) \approx R_1 + R_2 + \frac{R_D R_S}{R_D + R_S}$, while above the resonance the real part goes to zero as all current runs through the capacitance's, $Z(\omega) \approx \frac{-i}{(C_J+C)\omega}$. Next, we turn our attention to the Josephson junction.

The principal equations of a Josephson junction are,

$$I(t) = I_c \sin \varphi(t), \quad \frac{d\varphi}{dt} = \frac{\hbar}{2e} V_J(t) \quad (6)$$

with $V_J(t)$ being the junction voltage drop. Putting the junction in series with $Z(\omega)$ and a source at voltage V

yields

$$V = V_J(t) + \int d\tau Z_t(t - \tau) I_c \sin \varphi(\tau). \quad (7)$$

with $Z_t(t)$ being the Fourier transform of $Z(\omega)$. For $|V| \leq Z(0)I_c$ a trivial solution exists with a constant $\sin \varphi = \frac{V}{I_c Z(0)}$, corresponding to the supercurrent branch. However, since $Z(0) > \text{Re } Z(\omega)$ the circuit is underdamped with the possibility of multiple solutions. In a full treatment, finite temperature and noise would render parts of the supercurrent branch unstable with a switching voltage $V_{sw} \leq Z(0)I_c$. Here to simplify, we choose $V_{sw} = 0.46Z(0)I_c$ to match experiment and only consider solutions for $\varphi \neq \text{const.}$ at $|V| > V_{sw}$.

To obtain steady-state solutions after the switching one has to solve Eq. (7). This can be done numerically by Runge-Kutta method, shown in Fig. A.3(c), or analytically by keeping only the lowest harmonic of the Josephson frequency, $\omega_J/2\pi$, for which the phase is assumed to evolve as,

$$\varphi(t) = \omega_J t + \varphi_A \sin(\omega_J t + \delta), \quad (8)$$

in steady-state. Inserting this into Eq. (7), separating Fourier components, and keeping only the lowest order Bessel terms of $\sin \varphi(t)$, we find the following three equations,

$$V = \frac{\hbar}{2e} \omega_J + Z(0)I_c J_1(\varphi_A) \sin \delta, \quad (9)$$

$$\frac{J_0(\varphi_A)}{\varphi_A} = \frac{\hbar}{2e} \frac{\omega_J I_c}{|Z(\omega_J)|}, \quad (10)$$

$$\delta = -\arctan \left(\frac{\text{Re } Z(\omega_J)}{\text{Im } Z(\omega_J)} \right). \quad (11)$$

This can be further simplified by assuming φ_A to be small, and by Taylor expanding we find,

$$I_0 = I_c^2 \frac{e}{\hbar} \frac{\text{Re } Z(\omega_J)}{\omega_J}, \quad V = \frac{\hbar}{2e} \omega_J + Z(0)I_0, \quad (12)$$

with I_0 denoting DC current and matching Eqs. (2) of the main text. These equations can be jointly solved to obtain the I - V , shown as the full line in Fig. A.3(c). The perfect correspondence between numerical solutions of Eq. (7) and Eq. (12) supports this expansion. Lastly, we comment that an identical result to Eq. (12) can be obtained from $P(E)$ theory by expanding to lowest order in $\text{Re } Z(\omega)/R_K$, with $R_K = \frac{\hbar}{2e^2}$ denoting the resistance quantum, highlighting that the classical limit is justified [2, 3]. To obtain the DC power deposited in HEBs we use $P_j = R_j \langle I_j^2 \rangle_0$, with I_j being the current through HEB j , and index 0 indicating DC component. The full current and voltage drop across the junction is given by,

$$V_J(t) = \frac{\hbar}{2e} \omega_J - I_c \text{Re } Z(\omega_J) \sin(\omega_J t) - I_c \text{Im } Z(\omega_J) \cos(\omega_J t), \quad (13)$$

$$I(t) = I_0 + I_c \sin(\omega t), \quad (14)$$

using eqs. (12). The current through a HEB is then given by,

$$I_j(t) = I(t) - C_J \frac{dV_J}{dt} \quad (15)$$

which is used to obtain Eq. (3) of the main text. To note, for $\omega_J \gg \omega_{LC}$ all current runs through the capacitors and $I_j(t) \approx \frac{I_c}{1+C_J/C} \sin \omega_J t$, highlighting that the ratio C_J/C controls the distribution of power in this regime.

Next, we turn to the fitting of circuit parameters used in the main paper. First, the resistance of the thermometers is estimated to be $R_1 + R_2 = 30 \Omega$, and then from matching the supercurrent branch we find $R_S = 1920 \Omega$. Also, the junction capacitance with parallel line capacitance (between the junction and resistors) is geometrically estimated to be $C_J \approx 15$ fF. Next, there are two main features we utilize to extract parameters; 1) to fit the experimental $I-V$ we require an LC frequency $\omega_{LC}/2\pi \approx 93$ GHz and $R_D \approx 120 \Omega$ to place and broaden the resonance correspondingly, 2) to match the drop in power in regime 3 we require $C \approx 40$ fF. These requirements constrain the inductance to $L = 2.1$ nH, thereby

fixing all parameters. This value of L corresponds to a few mm long bonding wire. In general, the measurement of power allows us to determine the capacitive and inductive terms more precisely. This is highlighted in Fig. A.4 where we show multiple fits for the $I-V$'s of the main text. Here, the $I-V$'s are of almost equal quality, but plotting power for the same parameters reveals differences. Lastly, we highlight that the ratio of R_D to R_j determines the ratio of power absorbed by the HEBs, and the value of $R_D = 120 \Omega$, found by fitting $I-V$, fits well with the experiment, where we estimate this ratio to be $\sim 25\%$.

-
- [1] Jukka P. Pekola and Bayan Karimi, Colloquium: Quantum heat transport in condensed matter systems, *Rev. Mod. Phys.* **93**, 041001 (2021).
 - [2] Gert-Ludwig Ingold and Yu. V. Nazarov, Charge Tunneling Rates in Ultrasmall Junctions, arXiv.cond-mat/0508728
 - [3] Landry Bretheau, Localized Excitations in Superconducting Atomic Contacts: PROBING THE ANDREEV DOUBLET. PhD thesis, Ecole Polytechnique X, February 2013.

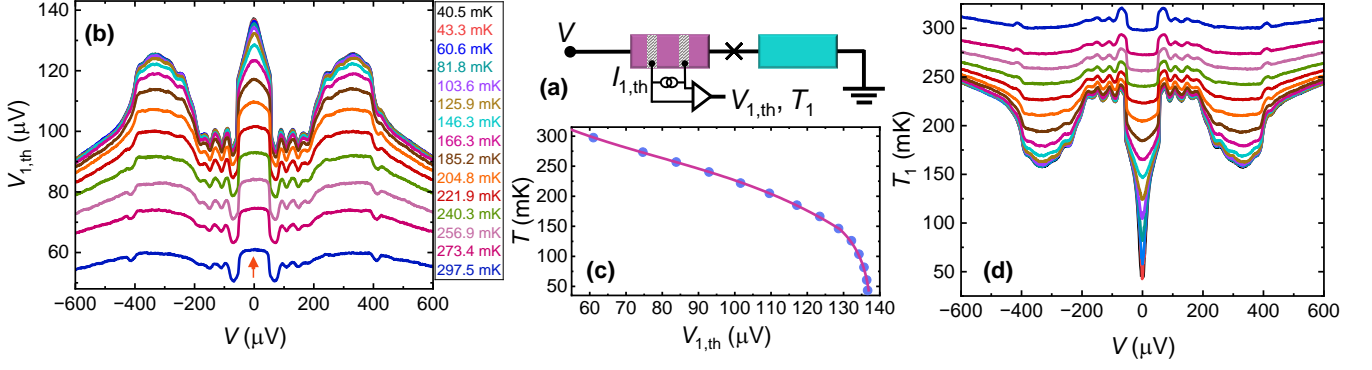


FIG. A.1. Temperature calibration of the voltage-biased JJ. (a) Current-biased measurement setup. The thermometer voltage $V_{1,\text{th}}$ is measured at a fixed current $I_{1,\text{th}} = 15$ pA as shown in (a) at different bath temperatures $T_0 = 43 - 298$ mK from top to bottom, against the voltage across the JJ. (d) The equilibrium values of $V_{1,\text{th}}$, at $V = 0$ (the position is shown by the red arrow in panel (c)), serves as the calibration $V_{1,\text{th}}(V = 0)$, versus T .

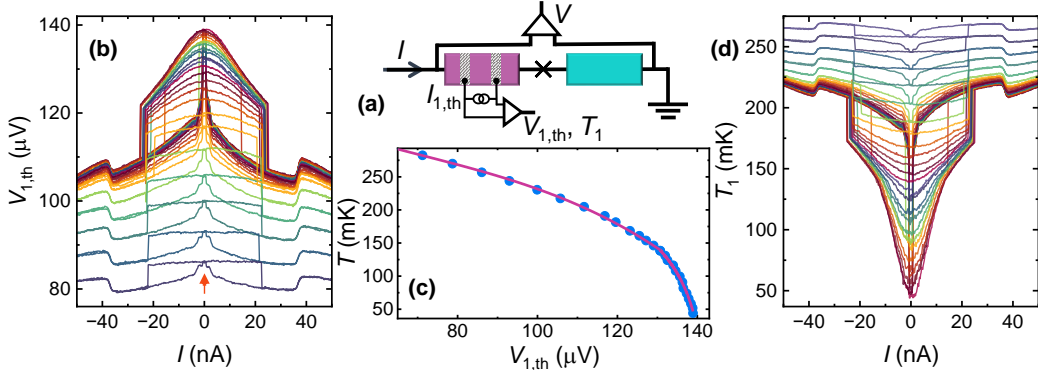


FIG. A.2. Temperature calibration of the current-biased JJ. (a) Current-biased measurement setup. The thermometer voltage $V_{1,\text{th}}$ is measured at a fixed current $I_{1,\text{th}} = 15$ pA as shown in (a) at different bath temperatures $T_0 = 43 - 256$ mK from top to bottom, against the current through JJ. (d) The equilibrium values of $V_{1,\text{th}}$, at $I = 0$ (the position is shown by the red arrow in panel (c)), serves as the calibration $V_{1,\text{th}}(I = 0)$, versus T .

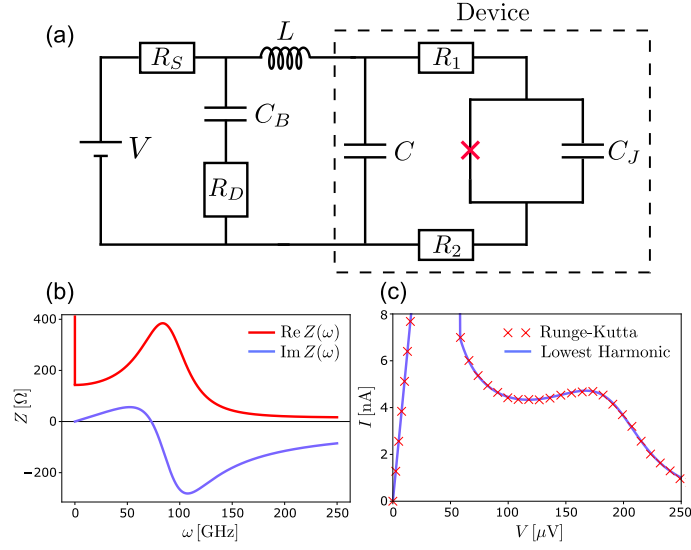


FIG. A.3. (a) Lumped element circuit used to model the experiment. The dashed section highlights the part of the circuit stemming from the device itself. (b) Impedance for the circuit in (a) using the fit parameters from the main text: $R_S = 1920 \Omega$, $R_1 + R_2 = 30 \Omega$, $R_D = 120 \Omega$, $C = 40 \text{ fF}$, $C_J = 15 \text{ fF}$, $C_B \rightarrow \infty$, $L = 2.1 \text{ nH}$, $I_c = 64 \text{ nA}$, $V_{sw} = 0.46Z(0)I_c$. (c) Theoretical I - V using parameters from (b). 'Runge-Kutta' is via solving Eq. (7) numerically, while 'Lowest Harmonic' is using Eq. (12).

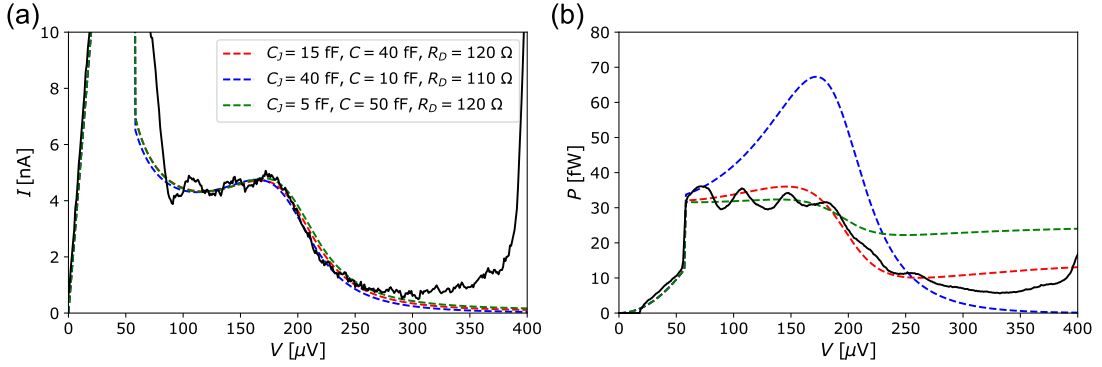


FIG. A.4. (a) I - V 's fitted to experiment for different values of C_J , C and R_D , with remaining parameters matching those in Fig. A.3(b). (b) Power absorbed in R_1 for the three parameter sets in (a), highlighting the importance of the C/C_J scale.